Inferring a photospheric velocity field from a sequence of vector magnetograms: The Minimum Energy Fit

D.W. Longcope

Montana State University, Dept. of Physics, Bozeman, MT 59717

ABSTRACT

We introduce a technique for inferring a photospheric velocity from a sequence of vector magnetograms. The technique, called *The Minimum Energy Fit*, demands that the photospheric flow agree with the observed photospheric field evolution according to the magnetic induction equation. It selects, from all consistent flows, that with the smallest overall flow speed by demanding that it minimize an energy functional. Partial or imperfect velocity information, obtained independently, may be incorporated by demanding a velocity consistent with the induction equation which minimizes the squared difference with flow components otherwise known. The combination of low velocity and consistency with the induction equation are desirable when using the magnetogram data and associated flow as boundary conditions of a numerical simulation. The technique is tested on synthetic magnetograms generated by specified flow fields and shown to yield reasonable agreement. It also yields believable flows from magnetograms of NOAA AR8210 made with the Imaging Vector Magnetogram at the Mees Solar Observatory.

Subject headings: Sun: photosphere — Sun: atmopheric motions

1. Introduction

Our understanding of the solar atmosphere has been greatly improved in recent decades through a combination of improved observational and computational techniques. Spectral polarimetry of optical absorption lines permit all three components of the magnetic field vector to be measured over the entire surface at which the spectral line is formed, typically the photosphere (see e.g. Stenflo 1994, for details on polarimetry). Successive advances have made it possible to obtain such data at ever increasing spatial resolution and time cadence. *Vector magnetograms* so produced offer the most significant observational data on the dynamics of the Sun's photospheric magnetic field and provide critical boundary data for any model of the coronal magnetic field.

The most realistic coronal field models are numerical solutions of the equations governing coronal dynamics. A typical such simulation solves the time-dependent equations of magnetohydrodynamics (MHD) within an active region corona subject to boundary conditions on the magnetic field and plasma velocity at the photospheric surface. Increasingly powerful computers and numerical techniques have made possible ever more faithful coronal models by allowing magnetograms to be used in the construction of their boundary conditions (Gudiksen & Nordlund 2002). A particularly ambitious and faithful coronal model would use time-dependent boundary conditions derived from a sequence of vector magnetograms along with a time-varying velocity field. One obstacle to producing such a model is that it is not yet possible to derive a photospheric flow field consistent with a given sequence of magnetograms.

Local Correlation Tracking (LCT, November & Simon 1988) is the most successful and most widely used method of inferring a horizontal velocity field $\mathbf{u}_h(\mathbf{x})$ from a sequence of images. The method was originally developed using sequences of intensity images $I(x, y, t_n)$ to derive a velocity between each successive pair. For each pair of images, an apodizing window centered at position $\mathbf{x}_0$, and nonzero within a small neighborhood, is used in a cross-correlation. The cross-correlation is expressed as a function of $\Delta\mathbf{x}$, the displacement applied to the first image. That displacement $\Delta\mathbf{x}_m$ which maximizes the cross-correlation yields a horizontal velocity for the central point of the apodizing window $\mathbf{u}_h(\mathbf{x}_0) = \Delta\mathbf{x}_m/\Delta t$.

The LCT will accurately recover the photospheric velocity provided, first of all, that the changes in the intensity are primarily caused by the velocity through advection

$$\frac{\partial I}{\partial t} + \mathbf{u}_h \cdot \nabla I \;=\; 0 \quad . \tag{1}$$

Optical photospheric intensity is related to the local temperature $T(x, y)$ which does in fact obey an advection equation similar to (1). Another requirement of the LCT is that the velocity field be smooth on spatial and temporal scales sufficiently large to be approximated as constant over the interval Δt and within the apodizing window. If the velocity is also small enough then (1) can be approximately solved

$$I(\mathbf{x}, t + \Delta t) \;\simeq\; I[\mathbf{x} - \Delta t\mathbf{u}_h(\mathbf{x}),\, t] \quad . \tag{2}$$

Finally, the intensity image must contain structure on scales *small* enough that its autocorrelation has a distinguishable peak within the apodizing window. If this is the case than a cross-correlation between (2) and $I(\mathbf{x}, t)$ will peak at $\Delta\mathbf{x}_m \simeq \Delta t\mathbf{u}_h(\mathbf{x})$, which is the LCT velocity measurement.

More recently the LCT has been applied to line-of-sight magnetograms to recover the velocity field driving the evolution of active region magnetic fields (Chae 2001; Moon et al.

2002). This application is, however, problematic since magnetograms do not satisfy all of the conditions required for the LCT (Démoulin & Berger 2003). We grant for the moment that the magnetogram measures the vertical field component, $B_z(x, y)$, although this is only strictly true of a line-of-sight magnetogram if it is restricted to disk center. The vertical field evolves according to the magnetic induction equation

$$\frac{\partial B_z}{\partial t} + \mathbf{v}_h \cdot \nabla B_z \;=\; -\, B_z \nabla \cdot \mathbf{v}_h \;+\; \nabla \cdot (v_z \mathbf{B}_h) \quad , \tag{3}$$

rather than the horizontal, scalar advection equation, (1), assumed by the LCT. The terms on the right hand side (rhs) of expression (3) represent mechanisms other than simple advection by which vertical magnetic field may evolve. It is not clear that the first term, whereby horizontal convergence increases the field strength, will have a significant effect since the LCT uses the location of the cross-correlation peak but not its amplitude.

The principal source of difficulty in applying the LCT to magnetograms stems from the second term on the rhs of (3). According to this term, vertical flow may interact with the unmeasured, horizontal field to change B_z. It has been shown (Démoulin & Berger 2003) that standard LCT will attribute this change to a fictitious horizontal velocity; a pattern velocity not corresponding to fluid flow. Corrections have been proposed for the effects of vertical flow, provided vector magnetogram are available to specify all three components of $\mathbf{B}$ (Kusano et al. 2002; Welsch et al. 2004). Since the velocity component parallel to $\mathbf{B}$ does not affect its evolution, the proposed corrections assume it to be absent: $v_{\parallel} = 0$. This leaves only the two velocity components $\mathbf{v}_{\perp}$ perpendicular to the local field. Assuming the observed pattern velocity returned by LCT, $\mathbf{u}_h$, to be a projection of this, it is a simple matter to recover the actual fluid velocity, $\mathbf{v}_{\perp}$ including both its horizontal and vertical components.

The inference of photospheric velocity by applying the LCT to magnetograms, even after projection back to $\mathbf{v}_{\perp}$, has several potential drawbacks. The velocity found this way will not be consistent with the induction equation, since the induction equation was not used in its derivation. Moreover, it is not obvious how one may use a single equation, either (1) or (3), to specify both components of $\mathbf{v}_{\perp}$ independently. The LCT appears to overcome this deficit by demanding a separation in structure scales between $\mathbf{u}_h(x, y)$ and $I(x, y)$. The assumed separation, however, means the velocity field will not satisfy the induction equation over all scales. Since a numerical simulation will solve a form of the induction equation, the evolution of the interior will be inconsistent with any boundary evolution which combines magnetograms and LCT-derived velocity. This is likely to be an undesirable situation.

The present work introduces a method of using the induction equation to directly infer a photospheric velocity field consistent with a sequence of vector magnetogram. As the equation count above showed, this cannot be a unique result, and we explicitly show the

multiplicity of consistent velocities. We introduce a regularization which produces the unique velocity field with the smallest overall speeds which also satisfies the induction equation. The result is a velocity field we call the *minimum energy fit* (MEF), which is ideally suited to use as a boundary condition in numerical simulation. We derive the MEF algorithm in the next section and then test it against known solutions in the following section. Section 4 presents the results of applying the MEF to actual vector magnetograms of NOAA AR8210. We return, in the final section, to a discussion of the suitability of the inferred velocity as a boundary condition of numerical simulations.

2. Formulation of the method

Take the plane $z = 0$ to be the photospheric surface within which all three components of the magnetic field are measured. The magnetic field is assumed to evolve according to the ideal induction equation

$$\frac{\partial \mathbf{B}}{\partial t} \;=\; \nabla \times (\mathbf{v} \times \mathbf{B}) \quad . \tag{4}$$

The vertical component of this equation depends only on $\mathbf{v}$ and $\mathbf{B}$ in the photospheric plane, while the remaining components of the equation depend on vertical derivatives of these quantities as well. Therefore if a field $\mathbf{v}(x, y, 0, t)$ is found which is consistent with the vertical component of the equation

$$\nabla_h \cdot (v_z \mathbf{B}_h - B_z \mathbf{v}_h) \;=\; \frac{\partial B_z}{\partial t} \quad , \tag{5}$$

then the same velocity will also satisfy the remaining components of (4) given the proper choices of $\partial v_z/\partial z$, $\partial \mathbf{v}_h/\partial z$ and $\partial \mathbf{B}_h/\partial z$. Had the resistive induction equation been used instead of (4) the vertical diffusive term, $\eta \partial^2 B_z/\partial z^2$, would make it impossible to determine $\mathbf{v}$ from $\mathbf{B}$ measured within a single plane.

The magnetogram from time t_j will include several distinct regions $M_j^{(\nu)}$ in which $\mathbf{B}(\mathbf{x}_h)$ is measured with sufficient accuracy to infer $\mathbf{v}$. In the simplest cases, measurements outside of these regions are consistent, to within measurement error, with $\mathbf{B} = 0$, and thus place no constraints on the velocity there. More generally the exterior will contain a mixture of zero and non-zero pixels whose structure is too complex for spatial derivatives to be reliably computed, making the interpretation of the induction equation impossible. Only inside the region can we hope to compute a photospheric velocity from the magnetogram. Nor can the velocity within one region be meaningfully related to that in any other based on the induction equation alone. Thus we find the velocity field within each region $M^{(\nu)}$ independently, and will henceforth consider a single region omitting the superscript.

Since the data consists of successive magnetograms from times t_j and t_{j+1} we must use finite differences to approximate the time derivative $\partial B_z/\partial t \simeq (B_{z,j+1} - B_{z,j})/\Delta t$. The optimal interval between magnetograms will be short enough that this finite difference is a good approximation, but long enough that ΔB_z can be accurately measured. Our objective is to find a steady velocity field $\mathbf{v}$ by which $\mathbf{B}_j$ will evolve to $\mathbf{B}_{j+1}$ over that time. Within the region $M \equiv M_j \cup M_{j+1}$ the field $\bar{\mathbf{B}} \equiv (\mathbf{B}_j + \mathbf{B}_{j+1})/2$ is accurately measured, and $\mathbf{v}$ can be found, in principle.

To solve eq. (5) for $\mathbf{v}_h$ and v_z we introduce unknown scalar potentials $\phi(\mathbf{x}_h)$ and $\psi(\mathbf{x}_h)$

$$v_z \mathbf{B}_h - B_z \mathbf{v}_h \;=\; \nabla_h \phi \;+\; \nabla_h \psi \times \hat{\mathbf{z}} \quad , \tag{6}$$

where $\mathbf{B}_h = (B_x, B_y)$ are the horizontal components of the measured magnetic field.[1] Substituting this decomposition into eq. (5) yields a Poisson equation for $\phi(\mathbf{x}_h)$

$$\nabla_h^2 \phi \;=\; \frac{\partial B_z}{\partial t} \quad . \tag{7}$$

This can be readily solved for ϕ inside M, given a suitable boundary condition on ∂M. Adopting the homogeneous boundary condition $\phi = 0$ at ∂M, does not compromise the generality of the solution, since transverse velocity components may be added through ψ.

The scalar potentials ϕ and ψ may be interpreted as generators of the inductive and electrostatic parts, respectively, of the horizontal electric field at the photosphere. Expressing the horizontal components of $\mathbf{E} = -\mathbf{v} \times \mathbf{B}$ using (6),

$$\mathbf{E}_h \;=\; -\,\hat{\mathbf{z}} \times (v_z \mathbf{B}_h - B_z \mathbf{v}_h) \;=\; \nabla \phi \times \hat{\mathbf{z}} \;-\; \nabla_h \psi \quad , \tag{8}$$

$\psi(x, y)$ appears as an electrostatic potential and $\phi(x, y)$ as a "stream function" generating the inductive, or divergence-free, electric field. According to this decomposition the electrostatic field plays no part in the evolution of B_z, and thus cannot be found from the induction equation. The *inductive potential* ϕ, on the other hand, is determined by the induction equation according to the Poisson equation (7).

---

[1] These are not the same as the components *transverse* to the line-of-sight, since the line-of-sight is rarely vertical. We assume throughout that the magnetogram data has been resolved into components which are locally vertical and horizontal.

2.1. The Minimization

Once the inductive potential $\phi(\mathbf{x}_h)$ has been found from eq. (7), the transverse velocity is given by

$$\mathbf{v}_h \;=\; \frac{1}{B_z}\left(v_z\mathbf{B}_h - \nabla_h\phi - \nabla_h\psi\times\hat{\mathbf{z}}\right) \quad . \tag{9}$$

This velocity satisfies the induction equation, (5), for all choices of $\psi(\mathbf{x}_h)$ and $v_z(\mathbf{x}_h)$. We are therefore free to impose additional constraints on the solution in order to uniquely specify these fields. These constraints might incorporate partial or imperfect information about the flow field, obtained by some other means. We express this independent velocity information as the *reference flow* $\mathbf{u}(\mathbf{x}_h)$, and set $\mathbf{u}=0$ when no independent information is available. In the end, however, we must consider the uses to which we will put the solution $\mathbf{v}$, and choose constraints which best suit that end.

The chief motivation of the inversion proposed here will be to find a velocity $\mathbf{v}$ to use as one boundary condition of a numerical simulation. From general properties of such simulations we expect large boundary velocities will be undesirable, and therefore seek the smallest possible velocity field consistent with equation (5). We define the smallest velocity as that which minimizes the functional

$$W\{\psi, v_z\} \;\equiv\; \tfrac{1}{2}\int_M \left[\,|\mathbf{v}_h-\mathbf{u}_h|^2 + |v_z-u_z|^2\right]\,dx\,dy \quad . \tag{10}$$

Since this functional resembles the kinetic energy (albeit within the photospheric plane), we call the resulting solution the *minimum energy fit*.

Demanding stationarity of W under variations of the field $v_z(\mathbf{x}_h)$, without variations in $\psi(\mathbf{x}_h)$, yields the Euler-Lagrange equation

$$v_z \;=\; \frac{B_z^2\,u_z \;+\; \mathbf{B}_h\cdot\left(\nabla_h\phi + \nabla_h\psi\times\hat{\mathbf{z}} + B_z\mathbf{u}_h\right)}{|\mathbf{B}|^2} \quad . \tag{11}$$

Alternatively, demanding stationarity under variations of $\psi(\mathbf{x}_h)$, while holding fixed $v_z(\mathbf{x}_h)$, yields a second Euler-Lagrange equation

$$\nabla_h\cdot\left(\frac{\nabla_h\psi}{B_z^2}\right) \;=\; \nabla_h\cdot\left[\frac{\hat{\mathbf{z}}\times\left(v_z\mathbf{B}_h - \nabla_h\phi - B_z\mathbf{u}_h\right)}{B_z^2}\right] \quad , \tag{12}$$

after integration by parts, and neglecting boundary terms. A pair of fields $\psi(\mathbf{x}_h)$ and $v_z(\mathbf{x}_h)$ which satisfy both (11) and (12) will make W stationary under simultaneous variations. Thus these equations are necessary but not sufficient conditions for minimizing the energy-like functional $W\{\psi, v_z\}$.

Substituting eq. (11) into eq. (12) gives a single partial differential equation for $\psi(x, y)$. With reference flow components $\mathbf{u}_h$ and u_z set to zero for simplicity, the resulting equation is

$$\nabla_h \cdot \left(\frac{\Pi \cdot \nabla_h \psi}{B_z^2} \right) = -\nabla_h \cdot \left[\frac{\Pi \cdot (\hat{\mathbf{z}} \times \nabla_h \phi)}{B_z^2} \right] \tag{13}$$

where the matrix

$$\Pi \;\equiv\; I \;-\; \frac{(\hat{\mathbf{z}} \times \mathbf{B}_h)(\hat{\mathbf{z}} \times \mathbf{B}_h)}{|\mathbf{B}_h|^2 + B_z^2} \tag{14}$$

is positive, semi-definite and acts as a projection onto the $\mathbf{B}_h$ direction wherever $B_z = 0$. Therefore, within regions $|B_z(\mathbf{x}_h)| > 0$, the electrostatic potential $\psi(x, y)$ solves a linear elliptic equation whose source term involves the inductive potential $\phi(x, y)$ and known magnetic field components.

Combining eqs. (9) and (11) it can be shown that $\mathbf{B} \cdot (\mathbf{v} - \mathbf{u}) = 0$ at all points on the surface. This is natural, since the MEF velocity minimizes the integral of

$$|\mathbf{v} - \mathbf{u}|^2 = |\mathbf{v}_\perp - \mathbf{u}_\perp|^2 + |\mathbf{v}_\parallel - \mathbf{u}_\parallel|^2 \quad , \tag{15}$$

subject to the induction equation, where $\mathbf{v}_\perp$ and $\mathbf{v}_\parallel$ correspond to the components of $\mathbf{v}$ perpendicular and parallel to the local magnetic field vector $\mathbf{B}$. The induction equation involves only $\mathbf{v}_\perp$, through the product, $\mathbf{v} \times \mathbf{B}$, and thus places no constraint at all on $\mathbf{v}_\parallel$. With no constraints, it is evident that setting $\mathbf{v}_\parallel = \mathbf{u}_\parallel$ will make the second term on the rhs of (15) its absolute minimum: zero. Any *independent* information about $\mathbf{v}_\parallel$, expressed through the reference flow $\mathbf{u}_\parallel$, is all the information there is, so the MEF velocity will have $\mathbf{v}_\parallel = \mathbf{u}_\parallel$.

A special case of the above result is that when no independent information about the flow is available, $\mathbf{u} = 0$, and the MEF velocity will be purely perpendicular to the magnetic field: $\mathbf{v} \cdot \mathbf{B} = 0$. We thereby see that the MEF is a generalization of the correction strategy used in application of LCT to magnetogram data (Kusano et al. 2002; Welsch et al. 2004). We use the term "generalization" since the MEF also adjusts one component of $\mathbf{v}_\perp$ by its minimization, while LCT appears to find this by demanding smoothness in the solution.

2.2. Solution Algorithm

We have produced a numerical implementation of the MEF in order to test the general technique. We use simple and straightforward iterative procedures to solve equations (7), (11) and (12). These procedures, described below in the interest of completeness, were adopted for their simplicity and are not intended to be the optimal solution scheme.

Fields $\bar{B}_z$ and $\partial B_z/\partial t$ are computed on each pixel of M from a pair of co-aligned vector magnetograms. Equation (7) is then solved for $\phi(x, y)$ at each pixel center using the boundary condition $\phi = 0$ on ∂M. By defining ϕ on pixel centers and ψ on pixel corners (vertices) the finite difference form of (5) will be satisfied exactly regardless of ψ or v_z. Further details on the differencing scheme are provided as an Appendix. Our implementation uses a centered-difference Laplacian and solves eq. (7) by standard Jacobi relaxation.

We next solve for $\psi(x, y)$ and v_z iteratively. In our first step we take $v_z(x, y) = u_z(x, y)$ and solve the elliptic equation eq. (12) for $\psi(x, y)$, using boundary conditions discussed below. Next we use the solution $\psi(x, y)$ in eq. (11) to compute $v_z(x, y)$. This field is used to re-compute $\psi(x, y)$, which is then used to re-compute v_z and so forth. In our experience this iterative procedure will eventually converge to solutions v_z and ψ which satisfy both eqs. (11) and (12) simultaneously. These are the Minimum Energy Fit to the observed magnetic evolution.

Elliptic equation (12) is solved within the domain M by Jacobi relaxation. The domain M is defined so that both $\mathbf{B}$ and $\partial B_z/\partial t$ vanish outside of it. It is therefore consistent to require that no flow cross the boundary: $\mathbf{v}_h \cdot \hat{\mathbf{n}} = 0$ on ∂M. We adopt this inhomogeneous Neumann condition on $\psi(x, y)$. Jacobi relaxation works fairly well in this case since there is almost always a very good initial guess for the solution from the previous iteration (before v_z was changed).

Equation (11) is algebraic for a continuous field $v_z(\mathbf{x}_h)$. We show in the Appendix that the variation of the discretized energy function yields a coupled, linear system of equations for the gridded values. Fortunately, the coupling matrix is diagonally dominant and the system may be solved by straight-forward relaxation techniques. We must therefore iterate to obtain a solution to (11), while holding fixed ψ.

It is troubling, at first sight, that our iterative procedure appears to introduce an artificial singularity. Equation (12) is singular where $B_z = 0$, even though the combined equation, (13) is singular only where $|\mathbf{B}| = 0$. It is extremely unlikely that $\bar{B}_z = 0$ exactly in any pixel, and we have rarely encountered anomalously large velocities for this reason. We do find, however, that system converges to a solution with layers of up-flows or down-flows localized to either side of the polarity inversion line (PIL, where $B_z = 0$) with little flow on the PIL. This feature may arise because the restriction of the elliptic operator, in eq. (13), inhibits coupling of the solution across the PIL. Another contributing factor may be the tendency, discussed in the Appendix, of the discretized version of eq. (11) to over-emphasize the smallest scales. We attempt to address this artifact by coupling the solution across the PIL using spatial smoothing. The converged velocity v_z is smoothed with a box-car filter, three to five pixels wide, and then used as the initial condition for a new set of relaxations. This

relaxation converges to a new solution which usually has a lower energy than the first and is more continuous across the PIL. This can be repeated, but there is generally less change with each repetition.

3. Tests of the MEF Algorithm

To demonstrate the effectiveness of the iterative inversion algorithm, and of the MEF principle, we apply it to two test cases. Each test case consists of a pair of synthetic magnetograms generated from the evolution of a magnetic field under the influence of a known *generating flow*. Applying the MEF to the pair of magnetograms results in an *inferred flow*. The inferred flow is not intended to match the generating flow since the defining criterion of the MEF, a minimum energy, will not be a property of the generating flow. A comparison of the two flows will, nevertheless, show the extent to which the MEF produces a flow with desirable properties and with a resemblance to reasonable photospheric flows. The test cases will also provide a means of exploring the effects of noise and the inclusion of independent flow information.

3.1. The Uniform Translation Test

For the first test we produce synthetic magnetograms from the rigid translation of classic spheromak magnetic field. The spheromak field is chosen because it is well-known (Bellan 2000), has few parameters and resembles, in certain respects, a bipolar active region with twisted flux. We use a spheromak confined within radius a, centered at $\mathbf{x}^{(c)}$, with positive helicity and a symmetry axis parallel to $\hat{\mathbf{x}}$. Vector magnetograms are synthesized by evaluating $\mathbf{B}$ within the plane $z = 0$ (see fig. 1a). The sphere center is translated from $\mathbf{x}_0^{(c)}$ to $\mathbf{x}_1^{(c)}$ while keeping the symmetry axis parallel to $\hat{\mathbf{x}}$. This motion is consistent with a uniform generating flow $\mathbf{v} = \mathbf{x}_1^{(c)} - \mathbf{x}_0^{(c)}$, when time is expressed in units of $\Delta t = t_1 - t_0$. For the purpose of comparison, the generating flow is taken to be the perpendicular part this uniform translation, $\mathbf{v}_\perp$.

The magnetic field is zero outside the sphere, so within each magnetogram $|\mathbf{B}| > 0$ within a circle. Figure 1a shows the synthetic magnetogram of $\bar{\mathbf{B}}$ for a case with $a = 20$ pixels, initially centered at $z_0^{(c)} = -3$ pixels (below the photosphere). This is displaced 4 pixels upward and 4 pixels Northwest (an angle of 35° from the x axis). The boundary of M is shown as a solid line, the transverse magnetic field by arrows, and the vertical field by grey-scale. Within this boundary the rigid displacement has an energy of $W_0 = 4.11 \times 10^4$,

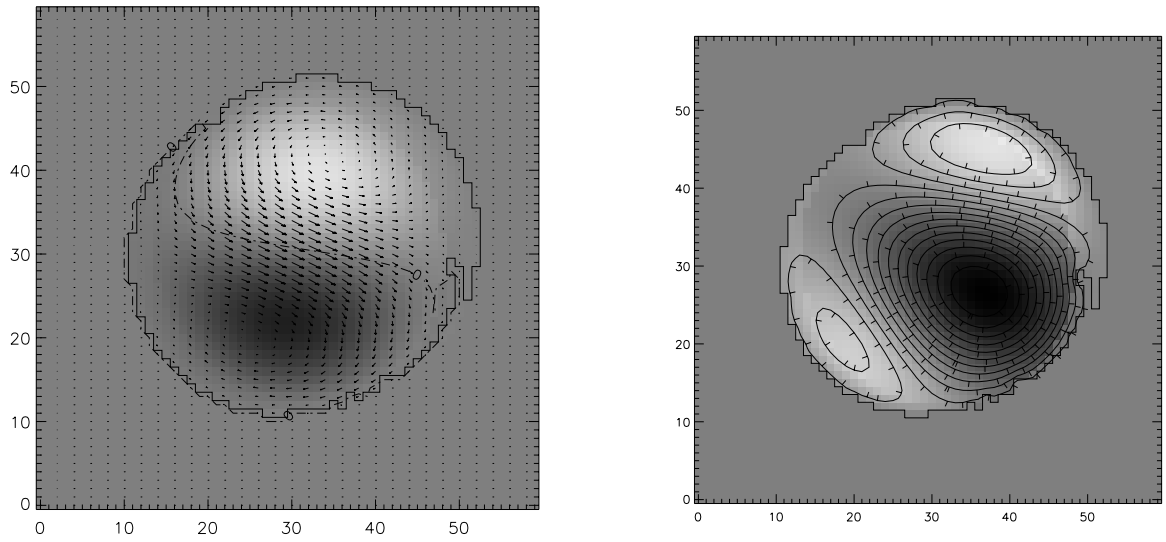

Fig. 1.— The input for the spheromak test case. (a) The synthetic vector magnetogram. Grey-scale shows the vertical field, $B_z(x, y)$, the broken curve is the PIL and arrows show $\mathbf{B}_h(x, y)$. (b) The dB_z/dt as a grey scale, and the inductive potential $\phi(x, y)$ shown in contours.

which is $|\mathbf{v}|^2 = 32$ over 1285 pixels.

Discarding parallel velocity components from the uniform flow, which could never be found, yields the photospheric flow shown in fig. 2a. This is the generating flow to which we compare the inferred flow. The generating flow has an energy $W_\perp = 2.7 \times 10^4$, which is naturally smaller than W_0, of the uniform translation. The flow is most upward near the PIL, where the magnetic field is most horizontal, and has a net upward flux of 3.1×10^3, smaller than that of the rigid motion: $4 \times 1285 = 5.1 \times 10^3$.

Invoking no independent flow information, $\mathbf{u} = 0$, and solving within the region M, beginning from $\psi = 0$, $v_z = 0$ we perform the alternating relaxation procedure described above. After ~ 800 iterations, relaxing either ψ or v_z, the system has nearly converged. The converged state is marked by undesirable up-flows localized to the either side of the PIL with almost no vertical flow on the PIL itself. This solution is smoothed and used to initiate another 300 iterations of relaxation. This converges to a solution with smooth up-flows and a lower energy. The smoothing and relaxation is then repeated, but with little noticeable change in the converged solution.

Figure 3 shows the evolution of the energy functional W during the relaxation. It is evident that both the ψ and v_z relaxations decrease the energy monotonically. Smoothing

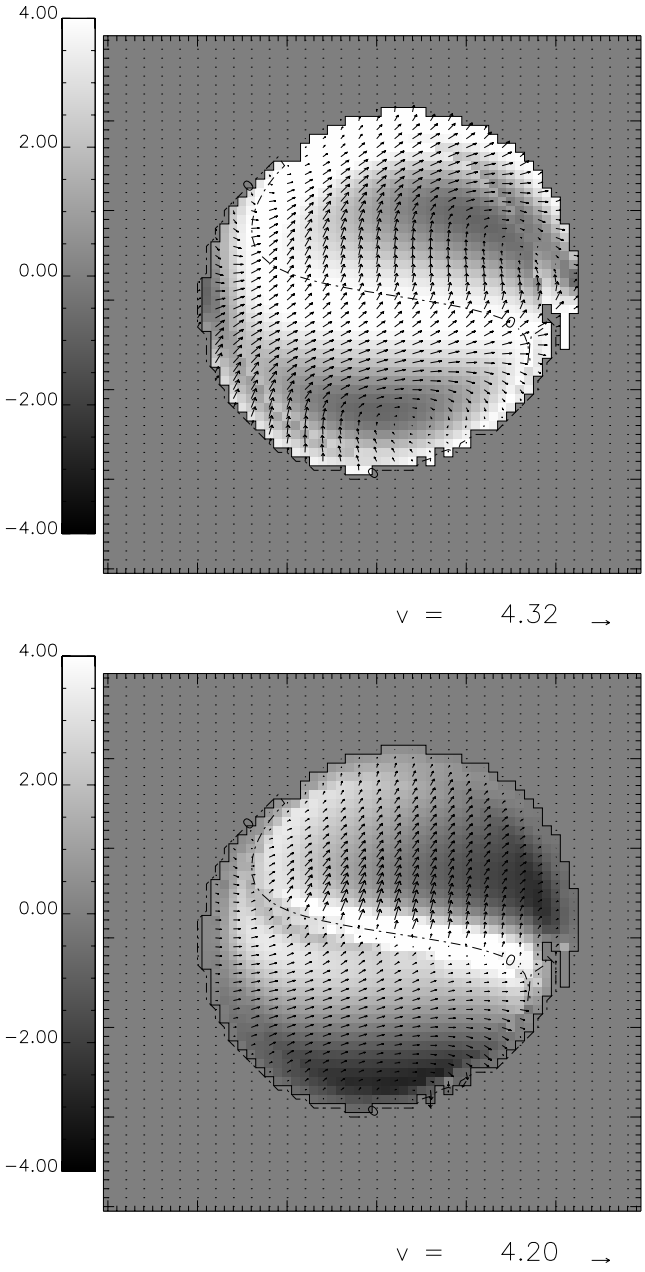

Fig. 2.— Flows corresponding to the emerging spheromak shown in fig. 1. Grey-scales show the vertical flow v_z, arrows show $\mathbf{v}_h$. The same scales for each are used in both panels. (a) The generating flow $\mathbf{v}_\perp$, the perpendicular components of a rigid translation, 4 pixels upward and 4 pixels along an axis 35° North of West (right). (b) The inferred flow from the MEF.

increases the the energy, but seems to permit subsequent relaxation to a solution with even lower energy. Each of the converged solutions has energy lower than $W_\perp$, the energy of the generating flow; the final energy of $W = 1.86 \times 10^4$, is the lowest achieved.

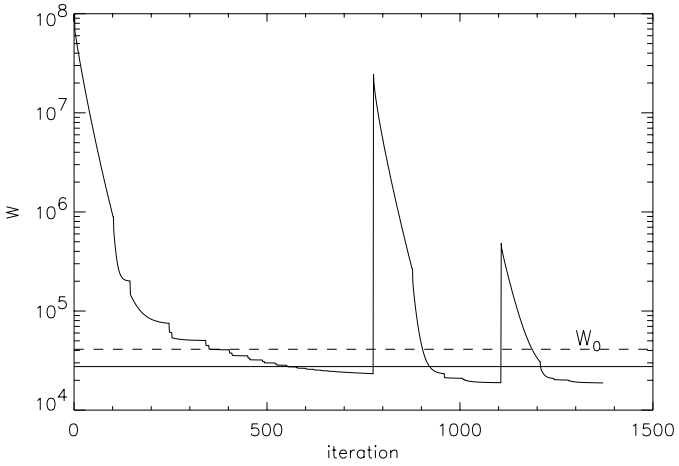

Fig. 3.— The energy functional W versus iteration in the alternating relaxation procedure. The relaxation decreases the solution below both reference energies W_0 (dashed) and $W_\perp$ (solid).

The inferred flow shown in figure 2b compares favorably with the generating flow $\mathbf{v}_\perp$. As described in an Appendix, the algorithm is constructed so that, to the level of round-off errors, the induction equation is satisfied regardless of variables v_z or ψ. Thus the inferred flow is a solution of the induction equation as legitimate as the generating flow. It is worthy of note that both flows agree in their general structure, with extended up-flows across the middle, and down-flow regions to the Northwest and to the South. The inferred horizontal flow is smooth and directed in similar direction and of comparable magnitude to the generating flow. The inferred velocity is more vertical at the PIL, but contains a significantly smaller net up-flow, 1.1×10^3, than the generating flow.

The two flow fields may also be compared by plotting, for each one, the vector field $\mathbf{f} = v_z \mathbf{B}_h - B_z \mathbf{v}_h$, which is related to the horizontal electric field $\mathbf{E}_h = \hat{\mathbf{z}} \times \mathbf{f}$. The vector field $\mathbf{f}$, computed according to expression (6), depends on the gradients of scalar potentials ϕ and ψ and not on the vertical velocity v_z. Since only the inductive potential ϕ is constrained by the induction equation, we can expect the two flows to differ in their respective electrostatic components, $\nabla_h \psi \times \hat{\mathbf{z}}$. The comparison in fig. 4 shows that the vector fields are very similar, but not identical.

The magnetic energy transported by the inferred flow is comparable to that of the

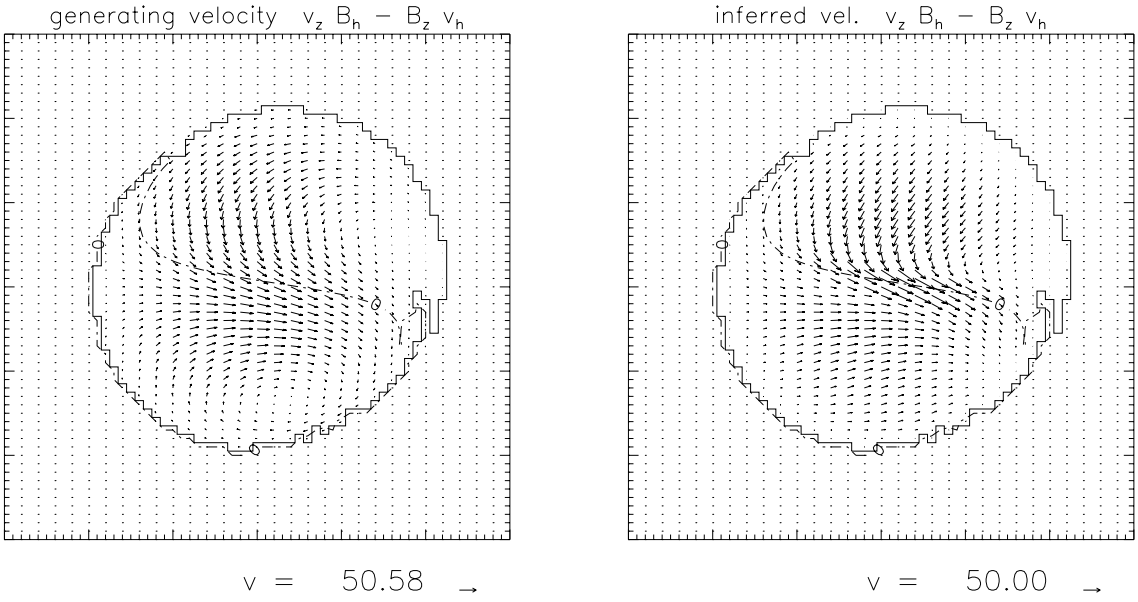

Fig. 4.— Plots of the vector field $\mathbf{f} = v_z\mathbf{B}_h - B_z\mathbf{v}_h$ for both the generating flow (a) and inferred flow (b).

generating flow. The integrated Poynting flux for any flow perpendicular to $\mathbf{B}$ gives a net power

$$P \;=\; \frac{1}{4\pi}\int \mathbf{B}\times(\mathbf{v}\times\mathbf{B})\cdot\hat{\mathbf{z}}\,dx\,dy \;=\; \frac{1}{4\pi}\int |\mathbf{B}|^2\mathbf{v}_\perp\cdot\hat{\mathbf{z}}\,dx\,dy \quad , \tag{16}$$

upwards across the $z = 0$ plane. The Poynting flux from the inferred flow, $P_{\rm MEF} = 6.2\times10^3$, only two thirds that of the generating flow, $P_0 = 9.4\times10^3$. At least in this case, the conservative assumption made my the MEF leads to a conservative estimate of the energy transport.

As a variant on this test we introduce the independent information about a uniform up-flow by setting the reference flow to $\mathbf{u} = 4\hat{\mathbf{z}}$. This modified inferred flow, shown in fig. 5a, has up-flow over the entire region, although it is not itself uniform. The net up-flow is 13% smaller than that of uniform up-flow. Apparently the horizontal flow associated with uniform up-flow (namely a uniform horizontal flow at $|\mathbf{v}_h| = 4$) has kinetic energy sufficiently large that the MEF opted to reduce it at the expense of a vertical mismatch. The energy of the inferred flow, $W = 1.57\times10^4$, is indeed lower than that of a purely horizontal flow, $W_0 = 1285\times16 = 2.06\times10^4$

To test its robustness we apply the MEF to magnetograms degraded with noise. To each component of the synthetic magnetograms used above we add uncorrelated, Gaussian random noise whose variance is $0.01\langle\, B_z^2\,\rangle$ (i.e. a 10% noise level). The degraded magnetograms are

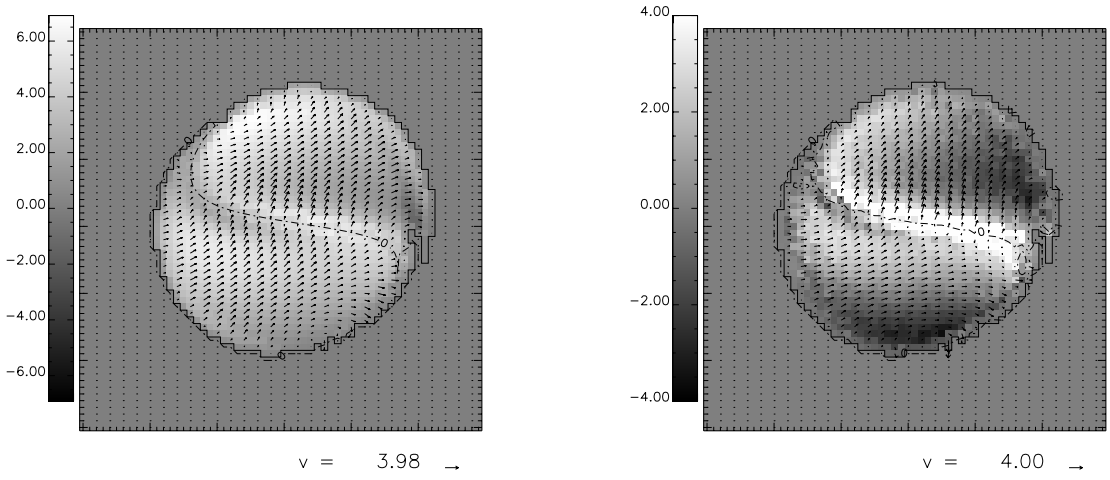

Fig. 5.— Variants on the test case. (a) MEF solution with the up-flow information included as $\mathbf{u} = 4\hat{\mathbf{z}}$. (b) The velocity inferred after noise has been added to each magnetogram.

combined to yield $\bar{\mathbf{B}}$ and ΔB_z. The MEF is applied to these within the same domain M used in the previous test. The result, shown in fig. 5b, is a reasonably good reproduction of the noise-free results. The energy function dropped to $W = 1.77 \times 10^4$, even lower than the noise-free case.

3.2. Test on Numerical Simulation Results

To test the MEF on a more complex generating flow we produce synthetic magnetograms from the results of a non-linear, time-dependent, three-dimensional, MHD simulation of flux emergence published by Magara and Longcope (2003). Figure 6a shows the averaged magnetogram generated from two time steps during a period slightly after the main emergence. Two distinct polarity regions are clearly visible connected by a sheared horizontal field. Figure 6b shows the simulation's velocity field at the same level from a time mid-way between the magnetograms.

The solid curve in fig. 6 shows the region M which includes both poles of the emerged flux tube separated by a PIL. The perpendicular component of this flow, shown in fig. 7a, has an energy $W_\perp = 2.5 \times 10^3$. The MEF algorithm yields a solution with slightly lower energy ($W = 1.7 \times 10^3$) shown in fig. 7b. This can be seen to share most of the features

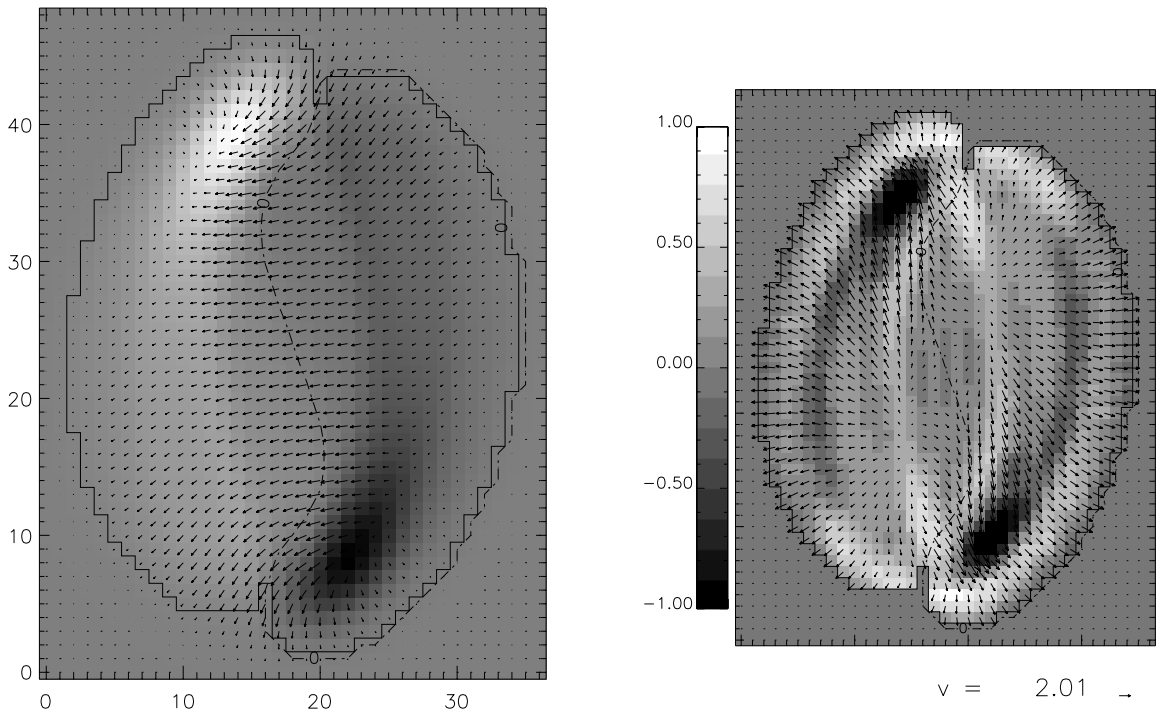

Fig. 6.— Synthetic data taken from the flux-emergence simulation of Magara and Longcope (2003). (a) The magnetogram averaged between times $t-18$ and $t=20$. (b) The simulation flow velocity from $t=19$.

with $\mathbf{v}_\perp$ from the simulation velocity. In particular, both have regions of up-flow around the periphery. The vertical flow in the MEF shows signs of a checkerboard pattern in regions of small B_z. This is a result of the small-scale enhancement discussed in the Appendix. Curiously, the simulation is still experiencing a positive Poynting flux, $P = 58$ at this stage, while the inferred flow transports energy downward: $P = -9.4$.

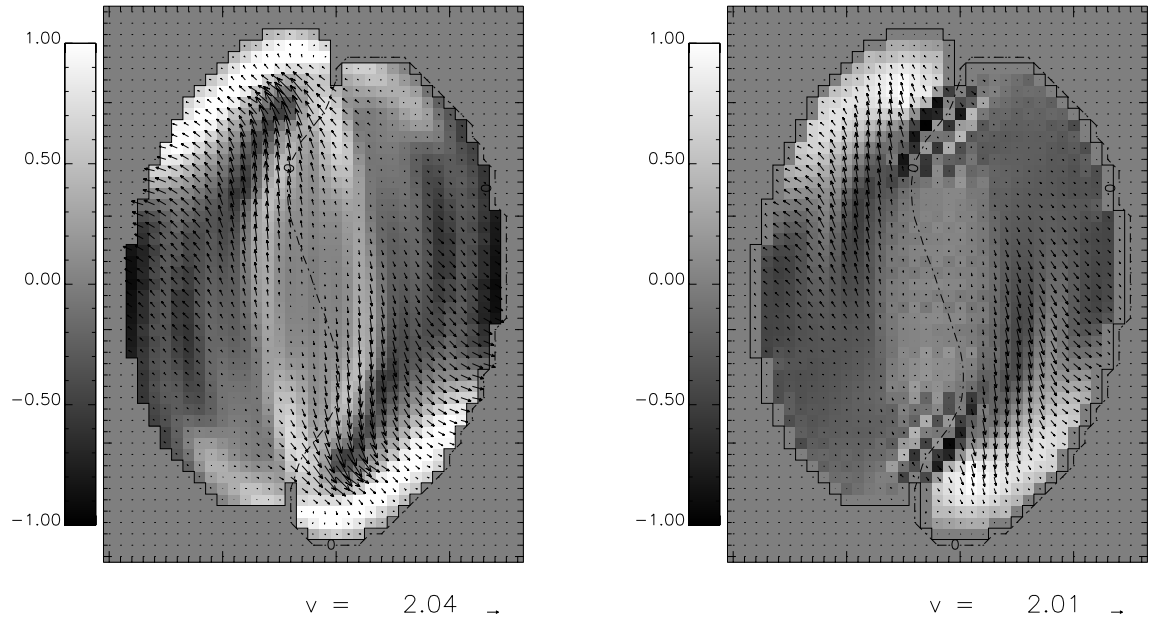

Fig. 7.— Photospheric flow velocities plotted with the same contour levels and arrow scalings. (a) $\mathbf{v}_\perp$ from the velocity in the self-consistent MHD simulation. (b) The velocity inferred applying MEF to the photospheric field evolution.

4. Application to Data

We demonstrate its capability on actual data by applying the MEF to a sequence of vector magnetograms made by the Imaging Vector Magnetograph (IVM, Mickey et al. 1996; Labonte et al. 1999) at University of Hawaii/Mees Solar Observatory. The data were acquired on May 1, 1998 of NOAA AR8210 (S16° E02°) at a time cadence of approximately three minutes. The resolution of the 180° ambiguity in the magnetic field component transverse to the line-of-sight, and the transformation to the heliographic coordinate system was performed using an automated iterative procedure (Canfield et al. 1993) which first minimizes the difference between the observed field and a force-free field computed using the B_z component and a force-free twist parameter "α", itself chosen as that for which the resulting ambiguity

resolution is least variable over the time series Leka & Barnes (2003); minimization of the divergence of $\mathbf{B}$ and of the vertical currents J_z follow for each magnetogram. Successive magnetograms are co-aligned with one-another using the cross-correlation of intensity maps, a technique which will minimize the motion of the "center of gravity" of the image, in this case the main sunspot. Random noise is then reduced by averaging the magnetic fields from five consecutive, co-aligned magnetograms. The time at the middle of this 15-minute sequence is used as the nominal time of the averaged magnetogram. We perform MEF analysis on pairs of averaged magnetograms separated by approximately 30 minutes. We consider two independent pairs, 18:38/19:09 and 19:48/20:19, from a period of relative quiet, between GOES flares observed at 17:54 and 22:54 (Sterling & Moore 2001), during which we expect relatively steady flow.

The first step of the MEF is to create a mean, $\bar{\mathbf{B}}$, and difference, ΔB_z, from the magnetogram pair. This averaging is intended to produce a field at the same time as the centered time difference, and should not be confused with the noise-reducing averaging performed in preparation for the MEF. Figure 8 shows the mean field and time derivative found using magnetograms from the first pair, 18:38/19:09. The sub-region M, selected using the threshold $|B_z| = 60G$, is shown as a solid perimeter in both panels.

Active region 8210 is dominated by a negative sunspot, observed to undergo clockwise rotation (Warmuth et al. 2000), to the East of which is an emerging flux region (EFR, Sterling et al. 2001). Our region M encloses the negative polarity of the sunspot, both polarities of the EFR, and several smaller positive flux concentration to its South. Within this region the positive flux, $\Phi_+ = 2.3 \times 10^{21}$ Mx, balances only a small fraction of the negative flux, $\Phi_- = 1.2 \times 10^{22}$ Mx; the remainder of 8210's positive polarity extends to the North and West and is therefore not included in M. The flux changes, shown as the grey-scale in 8b, increases the flux in each polarity at a rate of $\dot{\Phi} = 1.2 \times 10^{16}$ Mx/sec, primarily due to the emergence of the new flux. The transverse field is almost due North at the PIL, making the field *"inverse"* at the photospheric surface: it crosses the PIL from negative to positive. Movies of the vertical field reveal a generally Southward motion of the positive concentrations, but relatively little of the clockwise penumbral rotation seen in e.g. H-α (Warmuth et al. 2000).

The general features of both inferred flow fields, shown in fig. 9, are similar to one another and to expected evolution. The positive region is dominated by flow at ~ 300 m/sec following a Southward arc. There is very little motion in the negative region, even though fig. 8b shows the largest inductive electric fields, $|\nabla\phi|$, to be in this region; there is no hint of the clockwise sunspot rotation. At both times there is a down-flow, exceeding 400 m/sec, along the Northern portion of the PIL, accompanied by horizontal *outflows* (away from the

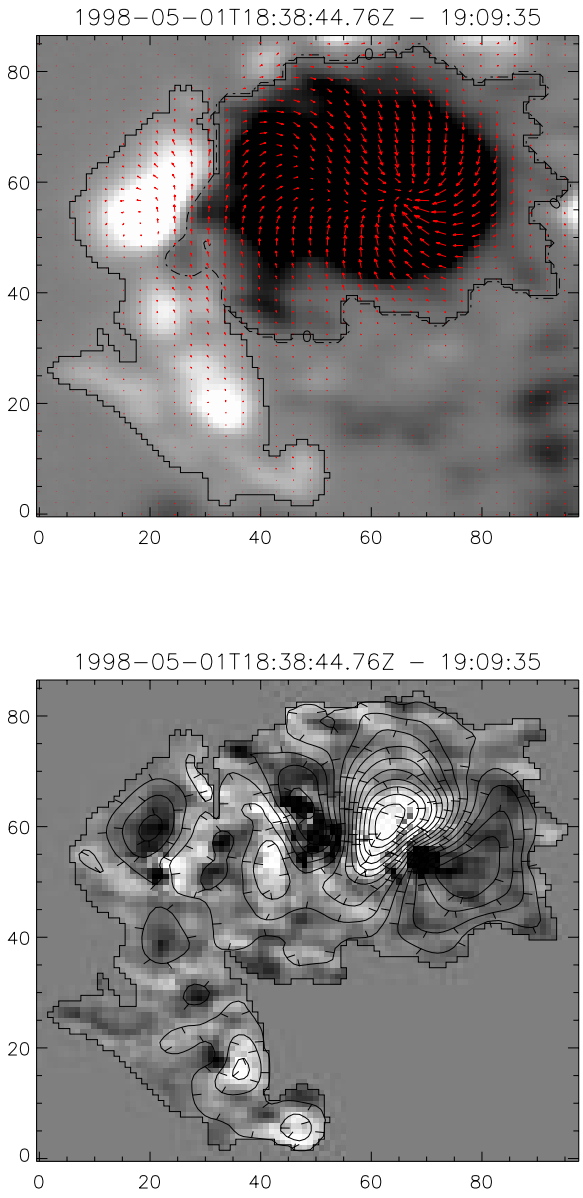

Fig. 8.— Magnetic field data from active region NOAA AR8210. (a) The mean magnetic field from magnetograms at 18:38 and 19:09. The region M is defined by the threshold $|B_z| \geq 60$ G. The grey-scale shows B_z on a scale truncated so that black to white, spans $B_z = -500$ G to $B_z = 500$ G. Arrows show the horizontal field $\mathbf{B}_h$. (b) The change ΔB_z between the two magnetograms. The full grey-scale spans $dB_z/dt = \pm 0.05$ G/sec, corresponding to a total difference $\Delta B_z = \pm 92$ G. The contours show the inductive potential $\phi(x, y)$, with dashes pointing "downhill".

PIL). This combination of down-flow and out-flow is natural when the opposing fluxes are augmented by PIL subduction of inverse field, which must be locally U-shaped. There is also a significant upflow throughout the center of the positive polarity; this presumably corresponds to the emerging flux.

There is no way to know the actual generating flow for this observed magnetic evolution. The analysis does, however, demonstrate that applying the MEF to actual data results in inferred flows with reasonable and repeatable properties. It is notable that magnetograms separated by just 30 minutes permit the inference of flows $\sim$ 200 m/sec over large regions (the Southward flow, for example). Advection at that speed will carry a photospheric fluid element only half way across a 1.1" pixel. These flows do, however, appear to be reliable since repeating the analysis with the outermost magnetograms (18:38/20:19) produces a flow-field resembling both 9a and 9b in form and magnitude. Active region 8210 is particularly well-studied because its complex evolution seemed to be responsible for a high level of activity including X-class flaring and coronal mass ejections (Warmuth et al. 2000; Sterling & Moore 2001). The MEF is nevertheless capable of inferring flows in even this abnormally complex region.

5. Discussion

The Minimum Energy Fit, presented here, infers a photospheric velocity field consistent with observed photospheric magnetic field evolution. The method determines a *set* of velocities, characterized by the single inductive potential ϕ, each member of which generates the observed evolution through the vertical component of the ideal induction equation. A single member of this set is selected by minimizing the energy functional $W\{\psi, v_z\}$. This minimization will not yield the *actual* photospheric velocity since the magnetic field evolution alone does not provide enough information to do so. Instead, the MEF returns *one possible* flow field, chosen to be the one with the least overall velocity (i.e. lowest kinetic energy) which is consistent with the observed magnetic evolution.

The minimization of W results in Euler-Lagrange equations for two other scalar fields, $\psi(x, y)$ and v_z. We have implemented the MEF by solving these equations using an alternating series of relaxations. We use this implimentation to demonstrate its capabilities by applying the MEF to magnetogram pairs synthesized from known field evolution and to pairs of actual magnetograms. When applied to synthetic magnetograms the inferred flow has good overall resemblance to, and still lower energy than, the generating flow. In the cases studied the inferred flow had smaller vertical Poynting flux and net mass flux than the generating flow. The algorithm, at least as presently implemented, converges most poorly

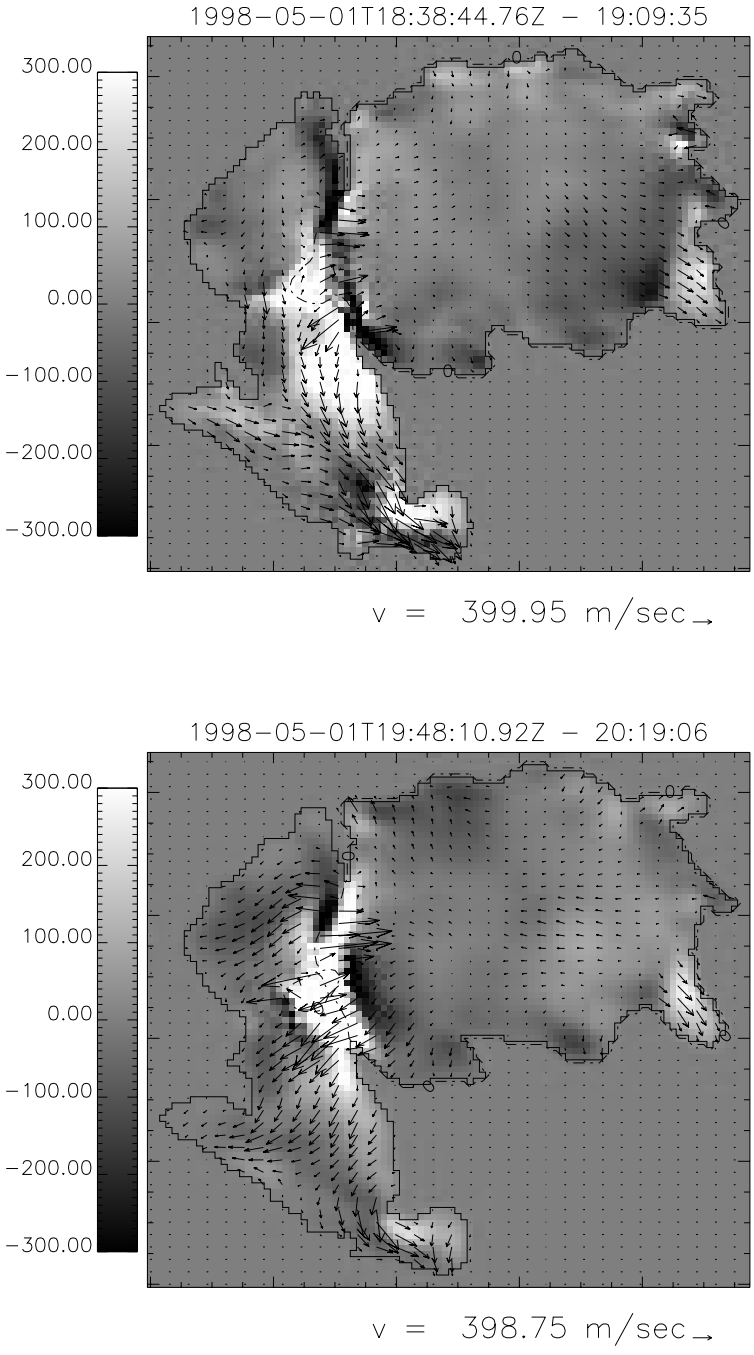

Fig. 9.— The result of MEF inversion. The reference arrows are each approximately 400 m/sec.

in the vicinity of the polarity inversion line. We find that repeated relaxation, interspersed with spatial smoothing aids the ultimate convergence.

The MEF approach has several advantages over Local Correlation Tracking and related velocity inference techniques. The MEF derives velocity directly from the ideal induction equation on a grid matching that of the magnetic field measurements. The result is a combined velocity/magnetogram sequence which is self-consistent and well-suited for use as a boundary conditions of a three-dimensional simulation. It adopts the conservative approach of finding the smallest velocities required for consistency with data.

Another advantage of the MEF is its capability of incorporating partial or imperfect velocity information obtained through independent means. Doppler shift measurements offer one potential source of this independent velocity information along the line of sight. Doppler shifts might be measured separately or from the same Stokes profile inversion used to derive the magnetic fields (see for example Skumanich & Lites 1987). The latter approach promises more consistency with the induction equation which involves the velocity acting on the measured magnetic field. An alternative use for the reference flow $\mathbf{u}$ is to use each velocity in a sequence to constrain the velocity of the subsequent step. This would amount to a solution which minimized, in some sense, changes in the velocity field. Finally, a separate application of the LCT, possibly to intensity images, might be used to constrain the horizontal flow fields in the MEF. This hybrid method would effectively combine the best aspects of both techniques. The MEF automatically projects away any parallel component, but also demands consistency with the induction equation.

The author wishes to thank K.D. Leka for supplying all the IVM data and for editing parts of the manuscript. He also thanks Tetsuya Magara for providing the results from his simulation, Stepahne Regnier for supplying earlier data files, and the anonymous referee for suggestions concerning the manuscript. Finally, he acknowledges the participants of the May, 2002 MURI workshop in Berkeley, particularly Isaac Klapper, Zoran Mikic, and Brian Welsch, for helping to initiate the work presented here. This work was supported by AFOSR under a DoD Multi-Universities Research Initiative (MURI) grant, "Understanding Solar Eruptions and their Interplanetary Consequences".

A. Finite Difference Formulation

The MEF algorithm is formulated on a grid defined by the pixels of the vector magnetogram. We assume this grid to be square and use the cell size as our unit of length. All components of the magnetic field $\mathbf{B} = (B_x, B_y, B_z)$ are assigned to the centers of the grid-

cells. Cell centers are indexed by integer pairs (i, j), and cell edges by half integers; $(i+\frac{1}{2}, j)$ is the vertical edge between cells (i, j) and $(i+1, j)$. Velocity components, $\mathbf{v} = (u, v, w)$ and scalar potentials ϕ and ψ are placed variously on cell centers, edges and vertices as illustrated in fig. 10. The derivatives of the scalar potentials define the vector

$$\mathbf{f} \;=\; (f, g) \;\equiv\; \nabla\phi + \nabla\psi \times \hat{\mathbf{z}} \quad , \tag{A1}$$

whose components are placed on cell edges and defined by the centered differences of the potentials

$$f_{i+\frac{1}{2},j} \;=\; \phi_{i+1,j} - \phi_{i,j} + \psi_{i+\frac{1}{2},j+\frac{1}{2}} - \psi_{i+\frac{1}{2},j-\frac{1}{2}} \quad , \tag{A2a}$$

$$g_{i,j+\frac{1}{2}} \;=\; \phi_{i,j+1} - \phi_{i,j} - \psi_{i+\frac{1}{2},j+\frac{1}{2}} + \psi_{i-\frac{1}{2},j+\frac{1}{2}} \quad . \tag{A2b}$$

The horizontal velocity components are computed on the same edges according to

$$u_{i+\frac{1}{2},j} \;=\; R_{i+\frac{1}{2},j}\left(\langle\, wB_x \,\rangle_{i+\frac{1}{2},j} - f_{i+\frac{1}{2},j} \right) \tag{A3a}$$

$$v_{i,j+\frac{1}{2}} \;=\; R_{i,j+\frac{1}{2}}\left(\langle\, wB_y \,\rangle_{i,j+\frac{1}{2}} - g_{i,j+\frac{1}{2}} \right) \tag{A3b}$$

where we introduce $\langle\, \cdot \,\rangle_{i+\frac{1}{2},j}$ to denote an average bringing cell-centered quantities onto edges

$$\langle\, wB_x \,\rangle_{i+\frac{1}{2},j} \;\equiv\; \tfrac{1}{2} w_{i+1,j} B_{x,i+1,j} + \tfrac{1}{2} w_{i,j} B_{x,i,j} \quad . \tag{A4}$$

For clarity we introduce the variable

$$R_{i+\frac{1}{2},j} \;\equiv\; \frac{1}{\langle\, B_z \,\rangle_{i+\frac{1}{2},j}} \quad , \tag{A5}$$

which is how the reciprocal of B_z will be defined on cell edges.

The velocity definitions (A3) have been chosen so that the discretized induction equation depends on ϕ alone, and may therefore be satisfied for arbitrary choices of $\psi_{i+\frac{1}{2},j+\frac{1}{2}}$ and $w_{i,j}$. The divergence is computed as a centered difference between all four edges

$$\begin{aligned} \left[\nabla \cdot (\mathbf{v}_h B_z)\right]_{i,j} \;=\; & u_{i+\frac{1}{2},j} \langle\, B_z \,\rangle_{i+\frac{1}{2},j} - u_{i-\frac{1}{2},j} \langle\, B_z \,\rangle_{i-\frac{1}{2},j} \\ & + v_{i,j+\frac{1}{2}} \langle\, B_z \,\rangle_{i,j+\frac{1}{2}} - v_{i,j-\frac{1}{2}} \langle\, B_z \,\rangle_{i,j-\frac{1}{2}} \quad . \end{aligned}$$

When definitions (A3) are used in this it follows that

$$\begin{aligned} \left[\frac{\partial B_z}{\partial t}\right]_{i,j} \;=\; & \left[\nabla \cdot (w\mathbf{B}_h - \mathbf{v}_h B_z)\right]_{i,j} \;=\; f_{i+\frac{1}{2},j} - f_{i-\frac{1}{2},j} + g_{i,j+\frac{1}{2}} - g_{i,j-\frac{1}{2}} \\ \;=\; & \phi_{i+1,j} + \phi_{i-1,j} + \phi_{i,j+1} + \phi_{i,j-1} - 4\phi_{i,j} \equiv \vec{\triangle}_{i,j} \cdot \vec{\phi} \quad , \end{aligned} \tag{A6}$$

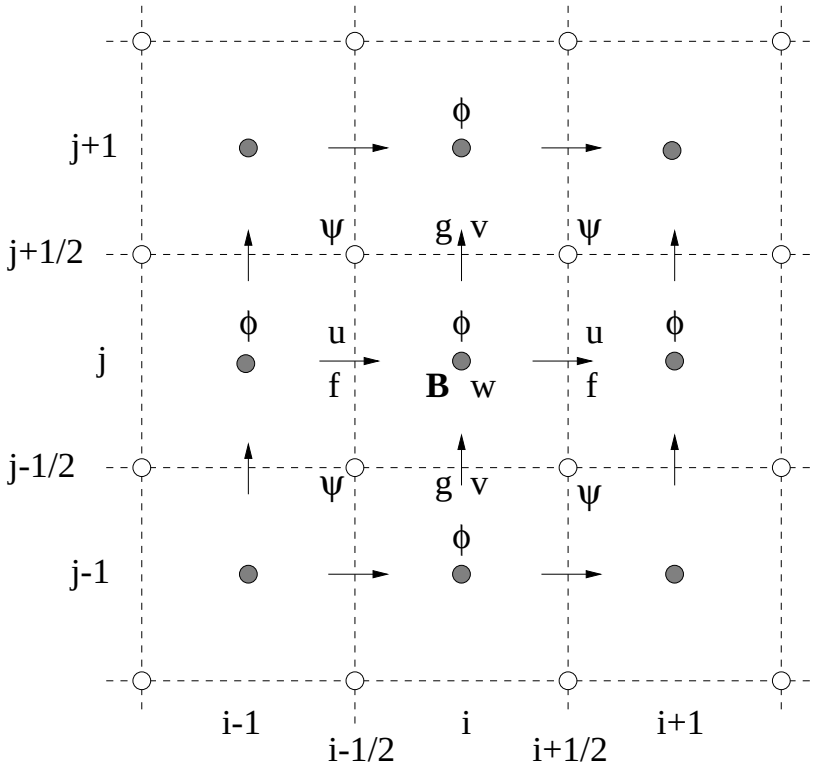

Fig. 10.— The computational grid and locations of the variables.

where $\vec{\triangle}_{i,j}$ is the finite-difference Laplacian at cell center (i,j). The induction equation is satisfied once $\phi_{i,j}$ solves the standard Poisson equation on a square grid. The boundary condition $\phi = 0$ on ∂M is enforced by setting $\phi_{i,j} = 0$ on all pixels outside the region M. Even if equation (A6) is solved only approximately, the induction equation is independent of the fields $\psi_{i+\frac{1}{2},j+\frac{1}{2}}$ and $w_{i,j}$, at least to the level of the round-off errors incurred when computing the telescoping sum.

Following the MEF derivation we specify the remaining quantities, $\psi_{i+\frac{1}{2},j+\frac{1}{2}}$ and $w_{i,j}$, by requiring that they minimize an energy functional. For clarity we show the numerical implementation of this minimization for the case with no *independent* velocity information, $\mathbf{u} = 0$. In place of the energy functional, (10), we use a sum over gridded quantities

$$W(\psi_{i+\frac{1}{2},j+\frac{1}{2}}, w_{i,j}) \;=\; \sum_{i,j} \Big[\, u^2_{i+\frac{1}{2},j} + v^2_{i,j+\frac{1}{2}} + w^2_{i,j} \,\Big] \quad . \tag{A7}$$

Performing a variation over $w_{i,j}$ yields

$$\begin{aligned}
\frac{\partial W}{\partial w_{i,j}} &= 2u_{i+\frac{1}{2},j}\frac{\partial u_{i+\frac{1}{2},j}}{\partial w_{i,j}} + 2u_{i-\frac{1}{2},j}\frac{\partial u_{i-\frac{1}{2},j}}{\partial w_{i,j}} + \\
&\quad + 2v_{i,j+\frac{1}{2}}\frac{\partial v_{i,j+\frac{1}{2}}}{\partial w_{i,j}} + 2v_{i,j-\frac{1}{2}}\frac{\partial v_{i,j-\frac{1}{2}}}{\partial w_{i,j}} + 2w_{i,j} \\
&= u_{i+\frac{1}{2},j}R_{i+\frac{1}{2},j}B_{x,i,j} + u_{i-\frac{1}{2},j}R_{i-\frac{1}{2},j}B_{x,i,j} + \\
&\quad + v_{i,j+\frac{1}{2}}R_{i,j+\frac{1}{2}}B_{y,i,j} + v_{i,j-\frac{1}{2}}R_{i,j-\frac{1}{2}}B_{y,i,j} + 2w_{i,j}
\end{aligned}$$

Setting this variation to zero, and substituting for u and v gives the coupled system of equations

$$\begin{aligned}
\vec{\mathcal{L}}_{i,j}\cdot\vec{w} &\equiv \tfrac{1}{4}R^2_{i+\frac{1}{2},j}B_{x,i,j}B_{x,i+1,j}w_{i+1,j} + \tfrac{1}{4}R^2_{i-\frac{1}{2},j}B_{x,i,j}B_{x,i-1,j}w_{i-1,j} \\
&\quad + \tfrac{1}{4}R^2_{i,j+\frac{1}{2}}B_{y,i,j}B_{y,i,j+1}w_{i,j+1} + \tfrac{1}{4}R^2_{i,j-\frac{1}{2}}B_{y,i,j}B_{y,i,j-1}w_{i,j-1} \\
&\quad + \tfrac{1}{4}[(R^2_{i+\frac{1}{2},j} + R^2_{i-\frac{1}{2},j})B^2_{x,i,j} + (R^2_{i,j+\frac{1}{2}} + R^2_{i,j-\frac{1}{2}})B^2_{y,i,j}]w_{i,j} + w_{i,j} \\
&= \tfrac{1}{2}(R^2_{i+\frac{1}{2},j}f_{i+\frac{1}{2},j} + R^2_{i-\frac{1}{2},j}f_{i-\frac{1}{2},j})B_{x,i,j} \\
&\quad + \tfrac{1}{2}(R^2_{i,j+\frac{1}{2}}g_{i,j+\frac{1}{2}} + R^2_{i,j-\frac{1}{2}}g_{i,j-\frac{1}{2}})B_{y,i,j} \quad .
\end{aligned} \tag{A8}$$

The finite-difference operator $\vec{\mathcal{L}}_{i,j}$ has a compact five-point stencil, and reduces to $|\mathbf{B}|^2/B_z^2$ in the continuum limit. The right hand side reduces to $\mathbf{B}_h \cdot \mathbf{f}/B_z^2$ in the continuum limit, yielding the algebraic equation (11). It is evident here that the discretized version of this algebraic equation is a coupled linear system in the unknown $w_{i,j}$. This system is solved by relaxation in our implementation of MEF, using a boundary condition that $w_{i,j} = 0$ in all pixels outside the region M.

The character of $\vec{\mathcal{L}}_{i,j}$ can be further clarified by considering the case of uniform magnetic fields. In that case the leading order expansion gives

$$\vec{\mathcal{L}}_{i,j} \;\rightarrow\; \frac{|\mathbf{B}|^2}{B_z^2}\left[\; 1 \;+\; \frac{B_x^2}{4|\mathbf{B}|^2}\frac{\partial^2}{\partial x^2} \;+\; \frac{B_y^2}{4|\mathbf{B}|^2}\frac{\partial^2}{\partial y^2} \;\right] \quad .$$

Inversion of this differential operator will tend to enhance high spatial frequencies, especially where B_z becomes small. This is a natural result of the fact that w enters the horizontal components of the energy through an average. Alternative formulations of equation (11), not based on minimization of the grid energy, have been found to be unstable. We therefore use eq. (A8) and suppress the highest frequencies of the result using a smoothing operation.

The final variation of the energy is

$$\begin{aligned}
\frac{\partial W}{\partial \psi_{i+\frac{1}{2},j+\frac{1}{2}}} &= 2u_{i+\frac{1}{2},j}\frac{\partial u_{i+\frac{1}{2},j}}{\partial \psi_{i+\frac{1}{2},j+\frac{1}{2}}} + 2u_{i+\frac{1}{2},j+1}\frac{\partial u_{i+\frac{1}{2},j+1}}{\partial \psi_{i+\frac{1}{2},j+\frac{1}{2}}} + \\
&\quad + 2v_{i,j+\frac{1}{2}}\frac{\partial v_{i,j+\frac{1}{2}}}{\partial \psi_{i+\frac{1}{2},j+\frac{1}{2}}} + 2v_{i+1,j+\frac{1}{2}}\frac{\partial v_{i+1,j+\frac{1}{2}}}{\partial \psi_{i+\frac{1}{2},j+\frac{1}{2}}} \\
&= -2u_{i+\frac{1}{2},j}R_{i+\frac{1}{2},j} + 2u_{i+\frac{1}{2},j+1}R_{i+\frac{1}{2},j+1} + \\
&\quad + 2v_{i,j+\frac{1}{2}}R_{i,j+\frac{1}{2}} - 2v_{i+1,j+\frac{1}{2}}R_{i+1,j+\frac{1}{2}}
\end{aligned}$$

Setting this variation to zero and substituting the velocity definitions (A3) yields another coupled set of equations. The operator in this case has a five-point stencil over vertices, and is a finite difference version of the second derivative in (12). The boundary condition of $\psi_{i+\frac{1}{2},j+\frac{1}{2}}$ is imposed by following the cell-edges bounding M and integrating ψ to assure that $\mathbf{v}_h \cdot \hat{\mathbf{n}} = 0$.

REFERENCES

Bellan, P. M. 2000, Sheromaks: A practical application of magnetohydrodynamic dynamos and plasma self-organization (Imperial College Press)

Canfield, R. C., et al. 1993, ApJ, 411, 362

Chae, J. 2001, ApJ, 560, L95

Démoulin, P., & Berger, M. A. 2003, Solar Phys., 215, 203

Gudiksen, B. V., & Nordlund, Å. 2002, ApJ, 572, L113

Kusano, K., Maeshiro, T., Yokoyama, T., & Sakurai, T. 2002, ApJ, 577, 501

Labonte, B., Mickey, D. L., & Leka, K. D. 1999, Solar Phys., 189, 1

Leka, K. D., & Barnes, G. 2003, ApJ, 595, 1277

Magara, T., & Longcope, D. W. 2003, ApJ, 586, 630

Mickey, D. L., Canfield, R. C., LaBonte, B. J., & Leka, K. D. e. a. 1996, Solar Phys., 168, 229

Moon, Y.-J., Chae, J., Choe, G. S., Wang, H., Park, Y. D., Yun, H. S., Yurchyshyn, V., & Goode, P. R. 2002, ApJ, 574, 1066

November, L. J., & Simon, G. W. 1988, ApJ, 333, 427

Skumanich, A., & Lites, B. W. 1987, ApJ, 322, 473

Stenflo, J. O. 1994, Astrophysics and Space Sciences Library, Vol. 189, Solar Magnetic Fields. Polarized radiation diagnostics (Kluwer Academic Publishers)

Sterling, A., & Moore, R. L. 2001, JGR, 106, 25,227

Sterling, A. C., Moore, R. L., Qiu, J., & Wang, H. 2001, ApJ, 561, 1116

Warmuth, A., Hanslmeier, A., Messerotti, M., Cacciani, A., Moretti, P. F., & Otruba, W. 2000, Solar Phys., 194, 103

Welsch, B. T., Fisher, G. H., Abbett, W. P., & Regnier, S. 2004, ApJ, Submitted